

This article has been published in: Journal of Dentistry 2018. pii: S0300-5712(18)30075-7. doi: 10.1016/j.jdent.2018.04.006.

Title: *In vitro* mechanical stimulation facilitates stress dissipation and sealing ability at the conventional glass ionomer cement-dentin interface.

Short title: Viscoelastic and chemical properties at glass-ionomer cements-dentin interface.

Authors: Manuel Toledano^{1*}, Raquel Osorio¹, Estrella Osorio¹, Inmaculada Cabello¹, Manuel Toledano-Osorio¹, Fátima S. Aguilera¹

Institution: ¹University of Granada, Faculty of Dentistry, Dental Materials Section.
Colegio Máximo de Cartuja s/n
18071 – Granada - Spain.

*Corresponding author: Prof. Manuel Toledano

University of Granada, Faculty of Dentistry

Dental Materials Section

Colegio Máximo de Cartuja s/n

18071 – Granada - Spain.

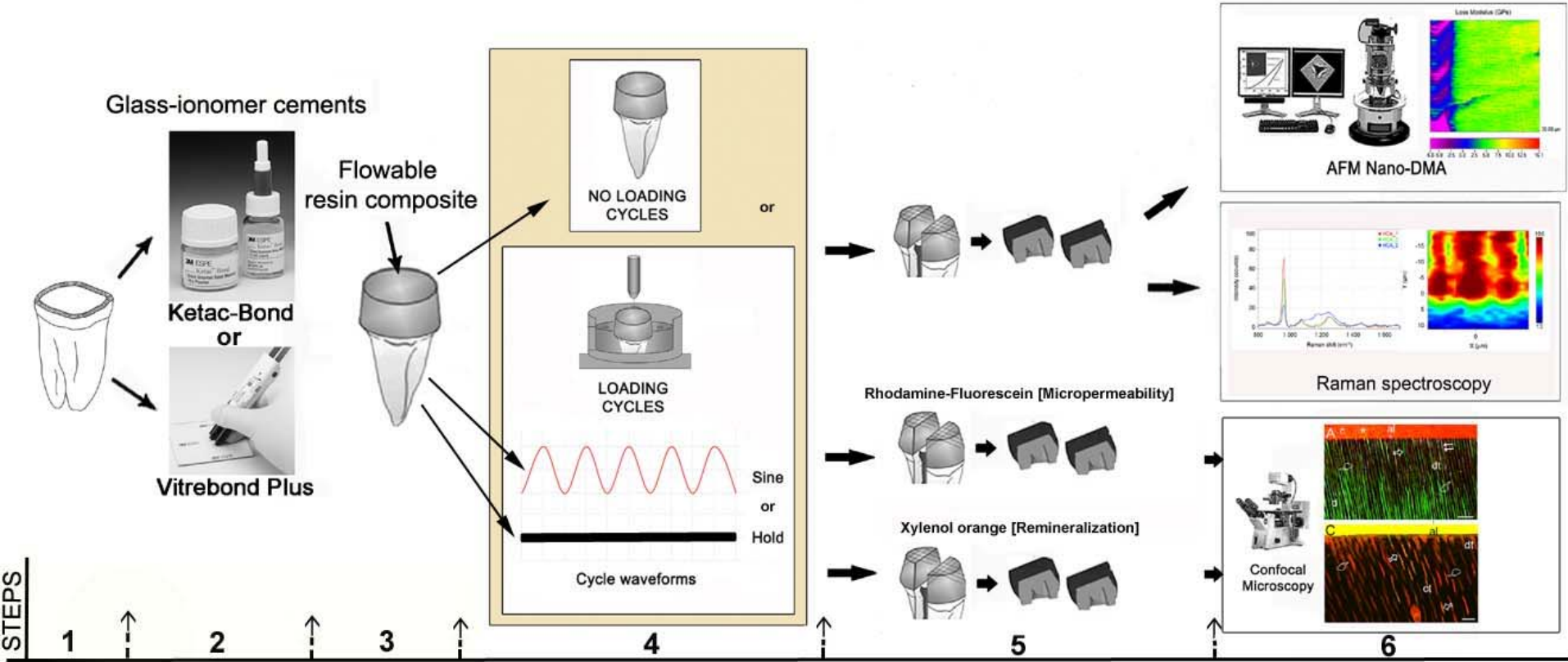
Tel.: +34-958243788

Fax: +34-958240809

Email: toledano@ugr.es

Keywords: chemical, dentine, interface, ionomer, Raman, viscoelastic.

Graphical abstract



Highlights

Dentin sealing of loaded GIC-bonded interfaces improved after loading.
After load cycling both class-ionomer cements favor dentin remineralization.
Mechanical stimuli facilitates stress dissipation at the GIC-dentin interface.

ABSTRACT

Objective: The aim of this study was to evaluate the induced changes in the chemical and mechanical performance at the glass-ionomer cement-dentin interface after mechanical load application.

Methods: A conventional glass-ionomer cement (GIC) (Ketac Bond), and a resin-modified glass-ionomer cement (RMGIC) (Vitrebond Plus) were used. Bonded interfaces were stored in simulated body fluid, and then tested or submitted to the mechanical loading challenge. Different loading waveforms were applied: No cycling, 24 h cycled in sine or loaded in sustained hold waveforms. The cement-dentin interface was evaluated using a nano-dynamic mechanical analysis, estimating the complex modulus and $\tan \delta$. Atomic Force Microscopy (AFM) imaging, Raman analysis and dye assisted confocal microscopy evaluation (CLSM) were also performed.

Results: The complex modulus was lower and $\tan \delta$ was higher at interfaces promoted with the GIC if compared to the RMGIC unloaded. The conventional GIC attained evident reduction of nanoleakage. Mechanical loading favored remineralization and promoted higher complex modulus and lower $\tan \delta$ values at interfaces with RMGIC, where porosity, micropermeability and nanoleakage were more abundant.

Conclusions: Mechanical stimuli diminished the resistance to deformation and increased the stored energy at the GIC-dentin interface. The conventional GIC induced less porosity and nanoleakage than RMGIC. The RMGIC increased nanoleakage at the porous interface, and dye sorption appeared within the cement. Both cements created amorphous and crystalline apatites at the interface depending on the type of mechanical loading.

Clinical significance: Remineralization, lower stress concentration and resistance to deformation after mechanical loading improved the sealing of the GIC-dentin interface. *In vitro* oral function will favor high levels of accumulated energy and permits micropermeability at the RMGIC-dentin interface which will become remineralized.

1. Introduction

Adhesive materials such as glass ionomer cements (GIC) have been clinically selected to accomplish dentin adhesion [1]. Formation of a shallow hybrid layers (HL) (~1-2 μm depth) made of cement and collagen [2,3] definitely contribute to micro and nano-mechanical bonding [4,5]. A volume of demineralized/unprotected collagen remains at the bottom of the hybrid layer (BHL) [6]. This vulnerable unsupported collagen may become the sites for collagen hydrolysis by host-derived matrix metalloproteinases (MMPs) enzymes [7] or by other proteases from bacteria [8] that may trigger the interface degradation [3].

Resin-modified glass-ionomer cements (RMGIC) set, when mixed, through an acid-base reaction between ion-leachable glasses and polyalkenoic acids, as well as upon light-polymerization of water-soluble (metha)crylate, such as HEMA [9]. Phosphate and calcium and lower fractions of aluminum, sodium or strontium have been previously measured at the cement-dentin interface [6]. They become integrated in this porous, non-particulate, poly(HEMA)-rich hydrogel layer [10], the absorption layer [11]. At the bottom of the absorption layer, hydroxyapatite that remained attached to individual collagen fibrils upon application of RMGIC forms receptors for primary chemical bonding with polyalkenoic acids incorporated into the materials [4,12]. The deposition of this submicron phase over the hybrid layer has also been evidenced and described in the conventional GICs-dentin interface. Thus, it can be regarded as a sub-layer of the earlier-documented absorption layer [11], identified as gel phase, gray intermediate layer or multilocular phase [4], which buffers the low pH [13]. This 7-10 μm thick structure [2] was first reported by Watson and Barlett (1994) [14], and contains some of the ions released by the initial acid-base glass-ionomer reaction between the fluoro-aluminosilicate glass particles, hydroxyapatite and polyacids. This structure is crucial for mediating the bond between RMGICs and dentin [2]. Intermediate and absorption layers have been thought to act as stress-breaking layers [15].

Chewing and occlusal loading can affect restorative strategies involving dentin. Teeth are continuously subjected to stresses during mastication, swallowing, and parafunctional habits. Weakly bonded tooth-material interfaces are more prone to suffer from the effects of oral environment in the short and long term [16]. Occlusal trauma is caused by conditions such as premature contacts, bruxism and clenching [17] and can affect both restorations and restorative strategies involving dentin. Thereby, minimally invasive dentistry comprises the philosophy of preservation of the maximum quantity of repairable dental tissues and utilizing remineralization approaches [18], to obtain the integrity of the cement-dentin interface. Previous chemico-mechanical studies have demonstrated that *in vitro* chewing and bruxism event have promoted resin-dentin interfaces highly infiltrated with resin with no presence of exposed demineralized collagen. This correlates with new mineral crystals embedded within a preserved collagen network. The mineral growing is associated with an increase in nano-hardness and Young's modulus [19].

The first nano-DMA and Raman-based characterization of dentin below GICs-based restorations is reported in the present manuscript. The tested null hypothesis is that there is no difference in chemical performance and stress dissipation of the cement-dentin interface created by a conventional glass ionomer cement and a resin-modified glass ionomer cement, after different *in vitro* mechanical stimuli.

2. Material and Methods

2.1. Specimen preparation, bonding procedures and mechanical loading

Thirty non-carious human third molars were obtained with informed consent from donors (20–40 year of age), under a protocol approved by the Institution Review Board (405/CEIH/2017). Molars were stored at 4°C in 0.5% chloramine T for up to 1 month before use. A flat mid-coronal dentin surface was exposed using a hard tissue microtome (Accutom-50; Struers, Copenhagen, Denmark) equipped with a slow-speed, water-cooled diamond wafering saw (330-CA RS-70300, Struers, Copenhagen, Denmark). A 180-grit silicon carbide (SiC) abrasive paper mounted on a water-cooled polishing machine (LaboPol-4, Struers, Copenhagen, Denmark) was used to produce a clinically relevant smear layer [20] [step 1, graphical abstract (GA)]. The specimens were divided into two main groups (n=15) based on the tested glass ionomer cement. A conventional glass ionomer cement, Ketac Bond (3M Deutschland GmbH, Neuss, Germany) and a resin-modified glass ionomer cement, Vitrebond Plus (3M Deutschland GmbH, Neuss, Germany) were employed (sep 2, GA). Glass ionomer cements were applied on dentin following the manufacturer's instructions, and a flowable resin composite (X-Flow™, Dentsply, Caulk, UK) was placed incrementally in five 1 mm layers and light-cured with a Translux EC halogen unit (Kulzer GmbH, Bereich Dental, Wehrheim, Germany) for 40 s (step 3, GA). The detailed composition and application mode are shown in Table 1.

The specimens were divided into three sub-groups, based on the type of mechanical loading that were applied: 1) Restored teeth stored in simulated body fluid solution (SBFS), for 24 h (no cycling). 2) Load cycling with sine waveform (259,200 cycles, 3 Hz,) (S-MMT-250NB; Shimadzu, Tokyo, Japan), and 3) Load with hold or sustained waveform, for 24 h (Instron 3345, Instron Corporation, Canton, MA, USA) (step 4, GA) (Figure S1). After performing the load cycling test, all specimens were kept in SBFS at 37 °C, until completing a total time of 24 h of immersion in SBFS.

To proceed with the mechanical loading of samples, specimens were mounted in plastic rings using dental stone. A compressive load of 225 N was applied to the flat resin composite build-ups using a 5-mm diameter spherical stainless steel plunger, while immersed in SBFS and proceeded as in Toledano et al., 2014 [21]. 225 N was selected as load cell (equivalent to “bite force”, *in vivo*) for all mechanical loading stimuli, as the mean peak bite force of all bruxism events has been reported to be 22.5 Kgf, with a duration of 7.1 s [22]. All specimens were longitudinally sectioned in 1.5-mm slabs from the central part of the specimen and polished through SiC abrasive paper from 800 up to 4.000-grit with a final polishing procedure performed with diamond pastes (Buehler-MetaDi, Buehler Ltd Illinois, USA), through 1µm down to 0.25µm (step 5, GA). The specimens were treated in ultrasonic bath (Model QS3, Ultrawave Ltd, Cardiff, UK) containing deionized water [pH 7.4] for 5 min at each polishing step.

2.2. Nano-DMA analysis and Atomic Force Microscopy analysis (AFM) imaging

Five slabs of restored teeth were submitted to nano-DMA and AFM analysis. Property mappings were conducted using a HysitronTi 950 nanoindenter (Hysitron, Inc., Minneapolis, MN) equipped with nano-DMA III, a commercial nano-DMA package. The nanoindenter tip was calibrated against a fused quartz sample using a quasistatic force setpoint of 5 µN to maintain contact between the tip and the sample surface. A dynamic (oscillatory) force of 5 µN was superimposed on the quasistatic signal at a frequency of 200 Hz. Based on a calibration-reduced modulus value of 69.6GPa for the fused quartz, the best-fit spherical radius approximation for tip was found to be 85 nm, for the selected nano-DMA scanning parameters. Modulus mapping of the samples was conducted by imposing a quasistatic force setpoint, $F_q=5 \mu\text{N}$, to which we superimposed a sinusoidal force of amplitude $F_A=1.8 \mu\text{N}$ and frequency $f=200 \text{ Hz}$. The resulting displacement (deformation) at the site of indentation was monitored as a function of time. Data from

regions approximately 50x50 μm in size were collected using a scanning frequency of 0.2 Hz. Viscoelastic data were acquired on the three different specimens and obtained from selected surface areas of the substrate using a rastering scan pattern. For each property map, 10 sets of 225 datapoints were used to obtain the median property value of a particular region of interest. That is, the 225 datapoints represent $1.47 \times 1.47 = 2.15 \mu\text{m}^2$ of each $30 \times 30 = 900 \mu\text{m}^2$ of the scan. The datapoints from 10 such non-overlapping squares were obtained for each zone at the bonded interface; thus, for each nano-DMA parameter, 30 values (3 specimens x 10 squares) were generated for each zone.

Under steady conditions (application of a quasistatic force) the indentation modulus of the tested sample, E , can be obtained by application of different models that relate the indentation force, F , and depth, D [23]. Complex modulus (E^*) and tan delta (δ) values were calculated as in Toledano et al. 2017 [24]. Measurements were recorded at the glass-ionomer cement layer (GI), on either the hybrid layer (HL) or bottom of hybrid layer (BHL), and on intertubular dentin (ID), as represented in the Figure S1. For intertubular dentin, discrete indentations were made in locations that were at least 3 μm from a peritubular cuff or previous indents. Statistical analysis was performed with ANOVA and Student Newman Keuls multiple comparisons tests. $P < 0.05$ was set for significance.

An atomic force microscope (AFM Nanoscope V, Digital Instruments, Veeco Metrology group, Santa Barbara, CA, USA) equipped with a Triboscope indenter system (Hysitron Inc., Minneapolis, MN) was employed in this study for topography analysis. The imaging process was undertaken inside a wet cell in a fully hydrated state (deionized water), using the tapping mode, with a calibrated vertical-engaged piezo-scanner (Digital Instrument, Santa Barbara, CA, USA). A 10-nm-radius silicon nitride tip (Veeco) was attached to the end of an oscillating cantilever that came into intermittent contact with the surface at the lowest point of the oscillation. Changes in vertical position of the AFM tip at resonance frequencies near 330 kHz provided the height of the images registered as bright and dark regions. 50 x 50 μm digital images were recorded from each resin-dentin interface, with a slow scan rate (0.1 Hz). To facilitate dentin surfaces observation, AFM images were tilted using a specific software (NanoScope Analysis v. 1.40, Bruker Corporation, Billerica, MA, USA) (step 6, GA).

2.3. Raman spectroscopy and hierarchical clusters analysis

The same dentin slabs were submitted to Raman analysis using a dispersive Raman spectrometer/microscope (Horiba Scientific Xplora, Villeneuve d'Ascq, France). A 785-nm diode laser through a X100/0.90 NA air objective was employed. Raman signal was acquired using a 600-lines/mm grating centered between 400 and 1700 cm^{-1} . Chemical mapping of the surfaces was performed. For each specimen, two areas 12x12 μm of the surfaces at different sites were mapped using 0.5 μm spacing at X and Y axis (625 points per map). The output from a clustering algorithm was basically a statistical description of the cluster centroids with the number of components in each cluster. The biochemical content of each cluster was analyzed using the average cluster spectra. The natural groups of components (or data) based on some similarity and the centroids of a group of data sets were found by the clustering algorithm once calculated by the software and the Hierarchical Cluster Analysis (HCA). The observed spectra were described at 400-1700 cm^{-1} with 10 complete overlapping Gaussian lines, suggesting homogeneous data for further calculations [25]. At this point, the mineral (relative presence of minerals and crystallinity) and the organic components (normalization, crosslinking, nature and secondary structure of collagen) of dentin was assessed as in Timlin et al., 2000 [26], Kunstar et al., 2012 [27] and Toledano et al., 2016 [28] (Step 6, GA).

2.4. Confocal microscopy evaluation

Additional teeth, 6 samples per group, were used in this part of the study. In half of the specimens, previous to the cement application, glass ionomers were doped with 0.05 wt% Rhodamine-B (RhB: Sigma-Aldrich Chemie GmbH, Riedstr, Germany). The pulpal chamber was filled with 1 wt% aqueous/ethanol fluorescein (Sigma-Aldrich Chemie GmbH, Riedstr, Germany) for 3 h [29,30]. The rest of the molars were immersed in 0.5 wt% xylenol orange solution (XO: Sigma-Aldrich Chemie GmbH, Riedstr, Germany), excited at 514-nm for 24 h at 37 °C (pH 7.2). Specimens were copiously rinsed with water and treated in an ultrasonic water bath for 2 min. The specimens were cut in resin-dentin slabs and polished using ascending grit SiC abrasive papers (#1200 to #4000) on a water-cooled polishing device (Buehler-MetaDi, Buehler Ltd. Lake Bluff, IL, USA). A final ultrasonic cleaning (5 min) concluded the specimen preparation. Analysis of bonded interfaces were performed by dye assisted confocal microscopy evaluation (CLSM), and attained by using a confocal laser scanning microscope (SP5 Leica, Heidelberg, Germany) equipped with a 20x, 40x and 60x oil immersion lenses. Fluorescein was activated by blue light (488-495 nm) and emitted yellow/green (520 nm), while the ultramorphology evaluation (cement-diffusion) was executed using Rhodamine excitation laser. Rhodamine was excited using green light (540 nm) and emitted red in color (590 nm). CLSM images were obtained with a 1 μm z-step to optically section the specimens to a depth up to 12-10 μm below the surface. The z-axis scans of the interface surface was arbitrarily pseudo-colored by the same operator for better exposure and compiled into single projections using the Leica image-processing software SP2 (Leica, Heidelberg, Germany). The resolution of CLSM images was 1024 x 1024 pixels. Five optical images were randomly captured from each resin-dentin interface, and micrographs representing the most common features of nanoleakage observed along the bonded interfaces were selected [31,32]. Fluorescences were or not separated into spectral regions, allowing that the operator has a full control of the region of the light spectrum directed to each channel (step 6, GA).

3. Results

3.1. Conventional glass ionomer cement (Ketac Bond)

Specimens submitted to load cycling attained lower complex modulus than the unloaded samples, in all zones of the cement-dentin interface. At both HL and bottom of the HL, $\tan \delta$ got the highest values when loading was performed in hold for 24 h. Differences among layers within the cement-dentin interface, when E^* and $\tan \delta$ were assessed, did not exist when loading in hold 24 h (Table 2). Both loading in sine and in hold 24 h favored mineralization, as the phosphate peaks and the mineral/matrix ratios were higher than in the unloaded group. Crystallinity attained the highest values, *i.e.*, the lowest full width half maximum (FWHM), at the bottom of the hybrid layer when specimens were loaded in sine (Table 3A). Similarly, the crosslinking of collagen (pyridinium) was greater after loading, though the highest values were achieved when sustained load (hold 24 h) was applied. Ratios concerning the secondary structure and organization of collagen (A-III, CH₂, A-I, Ratio A-I/A-III) attained higher Raman signals than the unloaded specimens, though amide III showed lower values after load cycling application (Table 3A).

At the conventional GIC bonded interfaces of the unloaded specimens, after multi-fluorescence examination, a rhodamine B-labeled adhesive layer (Fig. 1A-II) was completely affected by fluorescein penetration (nanoleakage) through the porous cement-

dentin interface (Fig. 1A·III). This conventional GIC-dentin interface also presented some local funneled dentinal tubules (Fig. 1A·I). Rhodamine B passed along the tubules through the hybrid zone, characterizing the interface with the presence of multiple cement tags (Fig. 1A·II). Specimens treated with conventional GIC loaded in sine, showed severe micropermeability and a porous hybrid layer, but moderate reflective signals at dentinal tubules. Mild nanoleakage signals were observed. Specimens bonded with conventional GIC and loaded in hold 24 h did not show signs of nanoleakage at the interface (Fig. 2A·I). Both scarce penetration of fluorescein throughout the dentinal tubules and water sorption within the thickness of the hybrid and intermediate layers were seen (Fig. 2A·III).

3.2. Resin-modified glass-ionomer cement (*Vitrebond Plus*)

Specimens submitted to load cycling showed higher complex modulus than the unloaded samples, in all zones of the cement-dentin interface, except when loading in hold 24 h. $\tan \delta$ showed greater values when loading in sine than in the rest of the groups, except at the cement zone. Important discrepancies among layers within the cement-dentin interface, when E^* and $\tan \delta$ were assessed appeared after loading in sine (Table 2). At both HL and bottom of the HL, loading in sine and in hold 24 h favored mineralization, as the phosphate peaks and the mineral/matrix ratios were greater than in the unloaded group. Crystallinity attained the highest values (*i.e.*, the lowest FWHM), when specimens were loaded in hold 24 h (Table 3B). Similarly, the crosslinking of collagen was greater after loading, though the highest values were achieved when sustained (hold 24 h) load was applied. Ratios concerning the secondary structure and organization of collagen followed irregular trend, though amide (A)-I and ratio A-I/A-III showed higher values when loading (Table 3B).

The fluorescent calcium-chelator dye xylenol orange determined a raise of mineralization at the cement-dentin interface when loading in sine. Mineral deposition, visualized by the fluorescent calcium-chelator dye technique, was observed within the hybrid layer and along some dentinal tubules (Fig. 3A). Strong pattern of micropermeability within the dentinal tubules and at the Rhodamine B-labeled cement was observed when samples were loaded in hold 24 h (Fig. S2A). The interface was characterized by a scarce presence of thin cement tags, and by moderate reflective signal inside the dentinal tubules, in the form of weak fluorescent structures.

4. Discussion

4.1. Conventional glass ionomer cement (*Ketac Bond*)

The tested null hypothesis, which reads “there is no difference in chemical performance and stress dissipation of the cement-dentin interface created by a conventional glass ionomer cement and a resin-modified glass ionomer cement, after different *in vitro* mechanical stimuli” must be rejected. This occurs as $\tan \delta$ was greater at the hybrid layer when specimens were mechanically loaded in sine (~1.2 fold) and sustained hold 24 h (~2 fold), than in the unloaded group. In general, an increased $\tan \delta$ was also determined at the bottom of the HL in all mechanical tests (Table 2). The lower $\tan \delta$, the greater the proportion of energy available in the system for recoil and/or failure [33], *i.e.*, better damping properties. On the other hand, $\tan \delta$ values higher than 1 represent liquid-like regions, contrarily to $\tan \delta$ values smaller than 1, that represent gel-like behavior to solid-like behavior as, $\tan \delta$ diverges [34]. The highest accumulation of energy, *i.e.*, the lowest dissipated energy or lowest $\tan \delta$, at the cement-dentin interface of Ketac Bond unloaded was described as a gap between the accumulated energy at the

HL and at the bottom of the HL (Fig. 1A). These two structures attained the greatest discrepant values of $\tan \delta$. A measure of the resistance of a material to dynamic deformation or robustness is given by the value of the complex modulus (E^*). Thus, the HL of the unloaded specimens attained a resistance to dynamic deformation of ~ 2 fold higher than both the glass ionomer cement layer and the bottom of the HL when Ketac Bond was applied (Table 2) (Fig. 1B). This result correlates well with greater stiffness [35]. The different resistance to deformation that was observed complies with deficiencies attained in dentin hybridization that provoked micropermeability and an unsealed cement-dentin interface (Fig. 1A·I).

When specimens treated with Ketac Bond were submitted to load cycling in sine, both area of the phosphate peak and mineral/matrix ratio were higher than in the unloaded group (Table 3A). FWHM values of the phosphate band was lower (~ 1.1 fold), in general, than in the unloaded samples (Table 3A). This greater mineralization and crystallinity [36], and the improved collagen organization (Table 3A) favored remineralization [12,37] at the cement-dentin interface. It was confirmed after examining the redder color, which corresponds to higher values of the locally measured phosphate peak (961 cm^{-1}) of the intensities map (Fig. S3B) in comparison with the unloaded group (Fig. S3A). It is speculated that the scarce capability to tightly seal the cement-dentin interface, might be supported in the viscoelastic performance of the different layers. Thus, cracks [38] at the interface were created, which would facilitate the dye pathway, and the formation of stick-slip images of nucleated minerals at the dentin, as sight of stress dissipation (Fig. S4) [39,40]. When specimens were loaded in sustained hold 24 h, E^* decreased ~ 1.5 fold the resistance to dynamic deformation at the interface (hybrid layer and bottom of the hybrid layer) respect to the cement layer (Table 2). Raman analysis confirmed the increase of mineralization due to the rise in height of phosphate (960 cm^{-1}) (PO_4^{3-} , ν_1) at the hybrid layer, and bottom of the hybrid layer (~ 4.8 and 2.7 fold, respectively). Similarly, the mineral/matrix ratio augmented after loading in sustained hold for 24 h, at both hybrid layer and bottom of the hybrid layer when phosphate was studied (Table 3A). In line with those findings, a general movement toward higher frequencies of crosslinking [Pyridinium (1032 cm^{-1})] was observable (Table 3A) after treatment with Ketac Bond load in hold 24 h. The ratio amide I/III which reflects the nature of collagen increased, in general, confirming advanced recovery of organic components and better collagen quality [37]. These changes are accompanied by an improved sealing of the cement-dentin interface (Fig. 2A·II). They also correlates with a decrease of hybrid layer porosity and remineralization (Fig. 2A·IV) (Table 3A) [31,41] at intertubular and peritubular dentin (Fig. 2B).

4.2. Resin-modified glass-ionomer cement (*Vitrebond Plus*)

When loading in sine waveform, the greater levels of accumulated energy (*i.e.*, the lowest $\tan \delta$ values) [33] at the interface, were not enough to produce any stick-slip formations as bridge-like structures at the dentin surface (Fig. 3B) as results of the homogenization of the viscoelastic properties [38]. Nevertheless, this might have contributed to *i)* lack of hermetic sealing at the interface, in close relationship with the greater levels of micropermeability that were attained (Fig. S5), and *ii)* an increase of dentin mineralization, especially stressed at peritubular level (Fig. 3B), but also at intratubular compartment. This was assumed after observing first, multiple reflective signal inside the dentinal tubules (Fig. S5), which indicated the presence of a solid mineral segment [31]; and second, after examining the redder color. Mineralization at the cement-dentin interface was confirmed after the Raman analysis, as phosphate (960 cm^{-1}) (PO_4^{3-} , ν_1) peak and area were higher when specimens loaded in sine were compared with the

unloaded group (Table 3B). This complies with a decrease of the mineral/matrix ratio (from 10.63 to 10.48 cm^{-1}) at the bottom of the HL (Table 3B). It also correlates with a strong discrepant $\tan \delta$ values between the HL (0.05 GPa) and the bottom of HL (0.10 GPa) (Table 2) which creates zones of stress concentration within the cement-dentin interface [33]. Therefore, the diffusion of fluorescein throughout this partially non infiltrated collagen, submitted to load cycling in sine, might have produced the poor sealing ability of Vitrebond Plus cement-dentin interface (Figs. 3A, S5). In general, the mineralization process was favored by the increase of the collagen crosslinking and a general improvement of the nature and secondary structure of collagen (Table 3B) [42].

A great degree of micropermeability and porosity of the interface, that permitted spectral overlap of both dyes, were observed at the cement-dentin interface submitted to 24 h of sustained loading (Fig. S2A). The lack of sealing of dentinal tubules permitted the leakage of fluorescein reaching the interface, which resulted partially occupied by scarcely mineralized and thin resin-modified cement tags (Figs. S2A, S2B). This performance was based on a general decrease of phosphate at dentin, though the crosslinking increase, in comparison with the unloaded specimens (Table 3B), helped for crystal precipitation [43]. In addition, indexes and ratios supporting the nature and secondary structure of collagen lowered. This confirmed the scarce scaffolding and the damage of conformation of the polypeptide chain, at the cement-dentin interface [37,44]. The cement-dentin interface was also characterized by a clear gap between both structures (Fig. S2B), and may have been originated in part as a consequence of dentin deformation after light curing application [45]. This gap permitted the passage of fluorescein toward the cement body, which was affected by dye sorption (Fig. S2A). Clinically, this passage will allow presence of bacteria and further degradation [7,8] and jeopardizing durability of the cement-dentin interface [31]. It is speculated that this breach might be a result of the stress concentration located at the limit between the dentin and the rest of the RMGIC-dentin interface, as $\tan \delta$ ranges from 0.32 GPa to ~ 0.17 , in general (Table 2). Nevertheless, these zones of stress concentration have been previously described in RMGIC, as well as in conventional GIC [46].

4.3. Conventional glass-ionomer cement vs resin-modified glass-ionomer cements

Raman analysis confirmed that higher dentin remineralization and crystallinity accounted when the conventional GIC was compared with the RMGIC in the unloaded specimens (Table 3). As a consequence, this growing of mineral deposits reduced porosity at the cement-dentin interface, after using GIC in the specimens without cycling. The interface obtained with the conventional glass ionomer cement (Ketac Bond) attained lower $\tan \delta$ values, than those achieved with the resin-modified glass ionomer cement (Vitrebond Plus), when specimens were not load cycled (Table 2). On the other hand, the complex modulus was greater at interfaces performed with Ketac Bond (GIC) than that obtained with Vitrebond Plus (RMGIC). From both measurements, it can be inferred that GIC-dentin interfaces (HL and bottom of the HL) have both higher proportion of energy available for recoil and/or failure [33], as well as higher resistance to deformation [35] than RMGIC-dentin interfaces. The clinical significance arising from these energetic states is supported on an increase in remineralization and higher mechanical properties [47] that were obtained at the cement-dentin interface of the unloaded specimens treated with the conventional glass ionomer. In general, the complex modulus was significantly lower at GIC-dentin interface than at RMGIC-dentin interfaces, after submitting the samples to the different mechanical stimuli. Furthermore, GIC-dentin interfaces showed higher $\tan \delta$ than RMGIC-dentin interfaces when mechanical loading was applied in sine and sustained hold for 24 h waveforms (Table 2). The degree and the quality of the

mineralization will affect the mechanical properties of dentin. Indeed, the extrafibrillar minerals act as a granular material that can withstand load, but in the absence of intrafibrillar mineralization. Intrafibrillar mineralization is the key factor for ensuring that collagen fibrils have the same high mechanical properties as occurs in natural biomineralized dentin [48]. Therefore, the increase of the mechanical performance of the infiltrated collagen, after using the RMGIC, is directly related to the precipitation of minerals at the dentin interface [49], and more specifically at the intrafibrillar compartment [48,50]. It is speculated that this increase of mineral precipitation at the intrafibrillar compartment concurred with poor extrafibrillar precipitation, allowing porosity and permeability at the cement-dentin interface when RMGIC was employed (Figs. S2, S4). On the contrary, the increase of the relative presence of minerals was attained when the GIC-dentin interface was load cycled (Table 3), in comparison with the unloaded specimens (Fig. 1A); it warranted the extrafibrillar mineralization. Thus, both porosity and micropermeability became reduced (Fig 2A). It should be noted that porosity has a direct effect on the permeability of bacteria and their products into dentin interfaces. From a clinical point of view, hermetic sealing is directly correlated to bacterial leakage [8]. Nevertheless, if viscoelastic response to deformation on a macro scale will be affected by the encountered subtle local property changes, should be elucidated; further research is required.

Complementary experimental techniques that ultimately illustrate the clinical behavior of dentin interfaces as Field-emission SEM (FESEM), dark-field TEM (DF-TEM), High Resolution TEM (HRTEM), Scanning Transmission Electron Microscopy (STEM), micro-XRD (μ -XRD) and longevity tests should have also been done. On the other hand, characterization of these new crystals that appeared at the dentin interface after mechanical loading, might be interesting to develop new composites based on this hydroxyapatite by bio-monitoring these data. Applying advanced technologies, both biofunctionality and biocompatibility studies should be carried out by using these starting crystals aimed to produce hydroxyapatite for therapeutic dental applications in regions of demineralized dentin. This approach also deserves future research.

5. Conclusions

1. A general trend to lower levels of accumulated energies (higher $\tan \delta$ values) and lower resistance to deformation (lower E^*) were assessed at the conventional GIC Ketac Bond-dentin interfaces when samples were submitted to mechanical loading. Load cycling applied on Ketac Bond-dentin interfaces facilitated sealing ability at the interface, creating stick-slip images of nucleated minerals at the dentin, acting as signs of stress dissipation. These changes became associated to reduced porosity and augmentation of amorphous minerals at the cement-dentin interface, which diminished the micropermeability.

2. The greater levels of accumulated energy at the Vitrebond Plus RMGIC-dentin interface submitted to loading in sine waveforms, produced lack of hermetic sealing and greater micropermeability at the interface. Nevertheless, dentin remineralization, based on both crystalline and amorphous apatite, augmented. Specimens treated with the RMGIC and loaded in hold for 24 h produced an increase of crystalline minerals. A gap within the cement-dentin interface permitted micropermeability and dye sorption of the cement layer. It produced a reduction of hermetic sealing at dentinal tubules.

3. GIC-dentin interface attained lower $\tan \delta$ values, *i.e.*, higher proportion of energy available at the interface, than that achieved with the RMGIC when specimens were not load cycled. The resistance to deformation, *i.e.*, complex modulus (E^*), was superior at interfaces infiltrated with the GIC Ketac Bond. Thereby, higher dentin

intrafibrillar remineralization was obtained when the conventional GIC was used without load cycling. Mechanical stimuli diminished the resistance to deformation and the energy stored in the system at the GIC-dentin interface, in comparison with the RMGIC.

Declaration of interests

The authors declare that they have no conflict of interest.

Acknowledgments

This work was supported by the Ministry of Economy and Competitiveness (MINECO) and European Regional Development Fund (FEDER) [Project MAT2017-85999-P].

References

- [1] T.F. Watson, A.R. Atmeh, S. Sajini, R.J. Cook, F. Festy, Present and future of glass-ionomers and calcium-silicate cements as bioactive materials in dentistry: biophotonics-based interfacial analyses in health and disease, *Dent. Mater.* 30 (2014) 50–61. doi:10.1016/j.dental.2013.08.202.
- [2] F.R. Tay, S.K. Sidhu, T.F. Watson, D.H. Pashley, Water-dependent interfacial transition zone in resin-modified glass-ionomer cement/dentin interfaces, *J. Dent. Res.* 83 (2004) 644–649.
- [3] M. Peumans, P. Kanumilli, J. De Munck, K. Van Landuyt, P. Lambrechts, B. Van Meerbeek, Clinical effectiveness of contemporary adhesives: a systematic review of current clinical trials, *Dent. Mater.* 21 (2005) 864–881. doi:10.1016/j.dental.2005.02.003.
- [4] E. Coutinho, Y. Yoshida, S. Inoue, R. Fukuda, J. Snauwaert, Y. Nakayama, J. De Munck, P. Lambrechts, K. Suzuki, B. Van Meerbeek, Gel phase formation at resin-modified glass-ionomer/tooth interfaces, *J. Dent. Res.* 86 (2007) 656–661.
- [5] N. Nakabayashi, A. Watanabe, K. Igarashi, AFM observation of collapse and expansion of phosphoric acid-demineralized dentin, *J. Biomed. Mater. Res. A.* 68 (2004) 558–565. doi:10.1002/jbm.a.20103.
- [6] M. Toledano, F.S. Aguilera, E. Osorio, I. Cabello, M. Toledano-Osorio, R. Osorio, Efficacy and micro-characterization of pathophysiological events on caries-affected dentin treated with glass-ionomer cements, *Int. J. Adhes. Adhes.* 69 (2016) 91–109. doi:10.1016/j.ijadhadh.2016.03.023.
- [7] R. Osorio, M. Yamauti, E. Osorio, J.S. Román, M. Toledano, Zinc-doped dentin adhesive for collagen protection at the hybrid layer, *Eur. J. Oral Sci.* 119 (2011) 401–410. doi:10.1111/j.1600-0722.2011.00853.x.
- [8] V. Biočanin, Đ. Antonijević, S. Poštić, D. Ilić, Z. Vuković, M. Milić, Y. Fan, Z. Li, B. Brković, M. Đurić, Marginal Gaps between 2 Calcium Silicate and Glass Ionomer Cements and Apical Root Dentin, *J. Endod.* (2018). doi:10.1016/j.joen.2017.09.022.

- [9] L. Chen, H. Shen, B.I. Suh, Bioactive dental restorative materials: a review, *Am. J. Dent.* 26 (2013) 219–227.
- [10] H. Cheng, W.J. Lederer, M.B. Cannell, Calcium sparks: elementary events underlying excitation-contraction coupling in heart muscle, *Science*. 262 (1993) 740–744.
- [11] S.K. Sidhu, T.F. Watson, Interfacial characteristics of resin-modified glass-ionomer materials: a study on fluid permeability using confocal fluorescence microscopy, *J. Dent. Res.* 77 (1998) 1749–1759.
- [12] C.K.Y. Yiu, F.R. Tay, N.M. King, D.H. Pashley, S.K. Sidhu, J.C.L. Neo, M. Toledano, S.L. Wong, Interaction of glass-ionomer cements with moist dentin, *J. Dent. Res.* 83 (2004) 283–289. doi:10.1177/154405910408300403.
- [13] H.C. Ngo, G. Mount, J. Mc Intyre, J. Tuisuva, R.J. Von Doussa, Chemical exchange between glass-ionomer restorations and residual carious dentine in permanent molars: an in vivo study, *J. Dent.* 34 (2006) 608–613. doi:10.1016/j.jdent.2005.12.012.
- [14] T.F. Watson, D.W. Bartlett, Adhesive systems: composites, dentine bonding agents and glass ionomers, *Br. Dent. J.* 176 (1994) 227–231.
- [15] S.K. Sidhu, P. Pilecki, P.-C. Cheng, T.F. Watson, The morphology and stability of resin-modified glass-ionomer adhesive at the dentin/resin-based composite interface, *Am. J. Dent.* 15 (2002) 129–136.
- [16] D. Erdilek, C. Dörter, F. Koray, K.-H. Kunzelmann, B.G. Efes, Y. Gomec, Effect of Thermo-mechanical Load Cycling on Microleakage in Class II Ormocer Restorations, *Eur. J. Dent.* 3 (2009) 200–205.
- [17] N. Noma, H. Kakigawa, Y. Kozono, M. Yokota, Cementum crack formation by repeated loading in vitro, *J. Periodontol.* 78 (2007) 764–769. doi:10.1902/jop.2007.060328.
- [18] H. Milly, F. Festy, T.F. Watson, I. Thompson, A. Banerjee, Enamel white spot lesions can remineralise using bio-active glass and polyacrylic acid-modified bio-active glass powders, *J. Dent.* 42 (2014) 158–166. doi:10.1016/j.jdent.2013.11.012.
- [19] M. Toledano, I. Cabello, F.S. Aguilera, E. Osorio, R. Osorio, Effect of in vitro chewing and bruxism events on remineralization, at the resin-dentin interface, *J. Biomech.* 48 (2015) 14–21. doi:10.1016/j.jbiomech.2014.11.014.
- [20] H. Koibuchi, N. Yasuda, N. Nakabayashi, Bonding to dentin with a self-etching primer: the effect of smear layers, *Dent. Mater.* 17 (2001) 122–126.
- [21] M. Toledano, F.S. Aguilera, I. Cabello, R. Osorio, Remineralization of mechanical loaded resin-dentin interface: a transitional and synchronized multistep process, *Biomech. Model. Mechanobiol.* 13 (2014) 1289–1302. doi:10.1007/s10237-014-0573-9.
- [22] K. Nishigawa, E. Bando, M. Nakano, Quantitative study of bite force during sleep associated bruxism, *J. Oral Rehabil.* 28 (2001) 485–491.
- [23] L. Han, A.J. Grodzinsky, C. Ortiz, Nanomechanics of the cartilage extracellular matrix, *Annu. Rev. Mater. Res.* 41 (2011) 133–168.

- [24] M. Toledano, R. Osorio, E. Osorio, A.L. Medina-Castillo, M. Toledano-Osorio, F.S. Aguilera, Ions-modified nanoparticles affect functional remineralization and energy dissipation through the resin-dentin interface, *J. Mech. Behav. Biomed. Mater.* 68 (2017) 62–79. doi:10.1016/j.jmbbm.2017.01.026.
- [25] J.W. Ager, R.K. Nalla, K.L. Breeden, R.O. Ritchie, Deep-ultraviolet Raman spectroscopy study of the effect of aging on human cortical bone, *J. Biomed. Opt.* 10 (2005) 034012. doi:10.1117/1.1924668.
- [26] J.A. Timlin, A. Carden, M.D. Morris, R.M. Rajachar, D.H. Kohn, Raman Spectroscopic Imaging Markers for Fatigue-Related Microdamage in Bovine Bone, *Anal. Chem.* 72 (2000) 2229–2236. doi:10.1021/ac9913560.
- [27] A. Kunstar, J. Leijten, S. van Leuveren, J. Hilderink, C. Otto, C.A. van Blitterswijk, M. Karperien, A.A. van Apeldoorn, Recognizing different tissues in human fetal femur cartilage by label-free Raman microspectroscopy, *J. Biomed. Opt.* 17 (2012) 116012. doi:10.1117/1.JBO.17.11.116012.
- [28] M. Toledano, R. Osorio, E. Osorio, F. García-Godoy, M. Toledano-Osorio, F.S. Aguilera, Advanced zinc-doped adhesives for high performance at the resin-carious dentin interface, *J. Mech. Behav. Biomed. Mater.* 62 (2016) 247–267. doi:10.1016/j.jmbbm.2016.05.013.
- [29] M. Toledano, F.S. Aguilera, S. Sauro, I. Cabello, E. Osorio, R. Osorio, Load cycling enhances bioactivity at the resin-dentin interface, *Dent. Mater.* 30 (2014) e169–188. doi:10.1016/j.dental.2014.02.009.
- [30] M. Toledano, E. Osorio, F.S. Aguilera, S. Sauro, I. Cabello, R. Osorio, In vitro mechanical stimulation promoted remineralization at the resin/dentin interface, *J. Mech. Behav. Biomed. Mater.* 30 (2014) 61–74. doi:10.1016/j.jmbbm.2013.10.018.
- [31] A.C. Profeta, F. Mannocci, R. Foxton, T.F. Watson, V.P. Feitosa, B. De Carlo, R. Mongiorgi, G. Valdré, S. Sauro, Experimental etch-and-rinse adhesives doped with bioactive calcium silicate-based micro-fillers to generate therapeutic resin-dentin interfaces, *Dent. Mater.* 29 (2013) 729–741. doi:10.1016/j.dental.2013.04.001.
- [32] M. Toledano, S. Sauro, I. Cabello, T. Watson, R. Osorio, A Zn-doped etch-and-rinse adhesive may improve the mechanical properties and the integrity at the bonded-dentin interface, *Dent. Mater.* 29 (2013) e142–152. doi:10.1016/j.dental.2013.04.024.
- [33] D.M. Espino, D.E.T. Shepherd, D.W.L. Hukins, Viscoelastic properties of bovine knee joint articular cartilage: dependency on thickness and loading frequency, *BMC Musculoskelet. Disord.* 15 (2014) 205. doi:10.1186/1471-2474-15-205.
- [34] H.H. Winter, Can the gel point of a cross-linking polymer be detected by the $G' - G''$ crossover?, *Polym. Eng. Sci.* 27 (1987) 1698–1702. doi:10.1002/pen.760272209.
- [35] H. Ryou, D.H. Pashley, F.R. Tay, D. Arola, A characterization of the mechanical behavior of resin-infiltrated dentin using nanoscopic Dynamic Mechanical Analysis, *Dent. Mater.* 29 (2013) 719–728. doi:10.1016/j.dental.2013.03.022.
- [36] K. Karan, X. Yao, C. Xu, Y. Wang, Chemical profile of the dentin substrate in non-carious cervical lesions, *Dent. Mater.* 25 (2009) 1205–1212. doi:10.1016/j.dental.2009.04.006.

- [37] H. Salehi, E. Terrer, I. Panayotov, B. Levallois, B. Jacquot, H. Tassery, F. Cuisinier, Functional mapping of human sound and carious enamel and dentin with Raman spectroscopy, *J. Biophotonics*. 6 (2013) 765–774. doi:10.1002/jbio.201200095.
- [38] A. Misra, P. Spencer, O. Marangos, Y. Wang, J.L. Katz, Parametric study of the effect of phase anisotropy on the micromechanical behaviour of dentin-adhesive interfaces, *J. R. Soc. Interface*. 2 (2005) 145–157. doi:10.1098/rsif.2005.0029.
- [39] C.S. Grimmer, C.K.H. Dharan, High-cycle fatigue life extension of glass fiber/polymer composites with carbon nanotubes, *J. Wuhan Univ. Technol., Mater Sci Ed*. 24 (2009) 167–173. doi:10.1007/s11595-009-2167-4.
- [40] R. Agrawal, A. Nieto, H. Chen, M. Mora, A. Agarwal, Nanoscale damping characteristics of boron nitride nanotubes and carbon nanotubes reinforced polymer composites, *ACS Appl. Mater. Interfaces*. 5 (2013) 12052–12057. doi:10.1021/am4038678.
- [41] M.C.G. Erhardt, M. Toledano, R. Osorio, L.A. Pimenta, Histomorphologic characterization and bond strength evaluation of caries-affected dentin/resin interfaces: effects of long-term water exposure, *Dent. Mater.* 24 (2008) 786–798. doi:10.1016/j.dental.2007.09.007.
- [42] C. Xu, Y. Wang, Cross-linked demineralized dentin maintains its mechanical stability when challenged by bacterial collagenase, *J. Biomed. Mater. Res. B Appl. Biomater.* 96 (2011) 242–248. doi:10.1002/jbm.b.31759.
- [43] M. Jastrzebska, R. Wrzalik, A. Kocot, J. Zalewska-Rejda, B. Cwalina, Raman spectroscopic study of glutaraldehyde-stabilized collagen and pericardium tissue, *J. Biomater. Sci. Polym. Ed*. 14 (2003) 185–197. doi:10.1163/156856203321142605.
- [44] C. Xu, Y. Wang, Collagen cross linking increases its biodegradation resistance in wet dentin bonding, *J. Adhes. Dent.* 14 (2012) 11–18. doi:10.3290/j.jad.a21494.
- [45] C.J. Soares, M.S. Ferreira, A.A. Bicalho, M. de Paula Rodrigues, S. Braga, A. Versluis, Effect of Light Activation of Pulp-Capping Materials and Resin Composite on Dentin Deformation and the Pulp Temperature Change, *Oper. Dent.* 43 (2018) 71–80. doi:10.2341/16-325-L.
- [46] S. Franco-Tabares, V.F. Stenport, L. Hjalmarsson, C.B. Johansson, Limited Effect of Cement Material on Stress Distribution of a Monolithic Translucent Zirconia Crown: A Three-Dimensional Finite Element Analysis, *Int. J. Prosthodont.* 31 (2018) 67–70. doi:10.11607/ijp.5469.
- [47] E. Coutinho, M.V. Cardoso, J. De Munck, A.A. Neves, K.L. Van Landuyt, A. Poitevin, M. Peumans, P. Lambrechts, B. Van Meerbeek, Bonding effectiveness and interfacial characterization of a nano-filled resin-modified glass-ionomer, *Dent. Mater.* 25 (2009) 1347–1357. doi:10.1016/j.dental.2009.06.004.
- [48] M. Balooch, S. Habelitz, J.H. Kinney, S.J. Marshall, G.W. Marshall, Mechanical properties of mineralized collagen fibrils as influenced by demineralization, *J. Struct. Biol.* 162 (2008) 404–410. doi:10.1016/j.jsb.2008.02.010.

- [49] Y. Li, T.T. Thula, S. Jee, S.L. Perkins, C. Aparicio, E.P. Douglas, L.B. Gower, Biomimetic Mineralization of Woven Bone-Like Nanocomposites: Role of Collagen Cross-Links, *Biomacromolecules*. 13 (2012) 49–59. doi:10.1021/bm201070g.
- [50] L.E. Bertassoni, S. Habelitz, J.H. Kinney, S.J. Marshall, G.W. Marshall, Biomechanical perspective on the remineralization of dentin, *Caries Res.* 43 (2009) 70–77. doi:10.1159/000201593.

Table 1. Materials and chemicals used in this study and respective manufacturers, basic formulation and mode of application

Product details		Basic formulation	Mode of application
Ketac Bond (3M Deutschland GmbH, Neuss, Germany)		<p><u>Ketac conditioner:</u> polycarboxylic (25% polyacrylic) acid, water (75%)</p> <p><u>Powder:</u> calcium-aluminum-lanthanum-fluorosilica glass, pigments.</p> <p><u>Liquid:</u> polycarboxylic acid, tartaric acid, water, conservation agents.</p>	<ul style="list-style-type: none"> - Apply Ketac conditioner (10 s) - Rinse with water. - Mix powder and liquid components. - Apply.
Vitrebond Plus (3M Deutschland GmbH, Neuss, Germany)		<p><u>Liquid:</u> resin-modified polyalkenoic acid, HEMA, water, initiators.</p> <p><u>Paste:</u> HEMA, Bis-GMA, water, initiators and radiopaque FAS.</p>	<ul style="list-style-type: none"> - Mix paste/liquid components (10-15s). - Apply. - Light activation (20s).
X-Flow™ (Dentsply, Caulk, UK)		Strontium alumino sodium fluorophosphorsilicate glass, di- and multifunctional acrylate and methacrylate resins, DGDMA, highly dispersed silicon dioxide UV stabilizer, ethyl-4-dimethylaminobenzoate camphorquinone, BHT, iron pigments, titanium dioxide.	
SBFS (pH=7.45)	Sigma Aldrich, St. Louis, MO, USA	NaCl 8.035 g NaHCO ₃ 0.355 g K ₂ HPO ₄ ·3H ₂ O 0.231 g, MgCl ₂ ·6H ₂ O 0.311 g 1.0 M – HCl 39 ml Tris 6.118 g	
	Panreac Química SA, Barcelona, Spain	KCl 0.225 g CaCl ₂ 0.292 g Na ₂ SO ₄ 0.072 g 1.0 M – HCl 0–5 ml	

Abbreviations: HEMA: 2-hydroxyethyl methacrylate; Bis-GMA: bisphenol A diglycidyl methacrylate; FAS: fluoraluminosilicate; DGDMA: diethyleneglycol dimethacrylate phosphate; BHT: butylated hydroxytoluene; SBFS: simulated body fluid solution; NaCl: sodium chloride; NaHCO₃: sodium bicarbonate; KCl: potassium chloride; K₂HPO₄·3H₂O: potassium phosphate dibasic trihydrate; MgCl₂·6H₂O: magnesium chloride hexahydrate; HCl: hydrogen chloride; CaCl₂: Calcium chloride; Na₂SO₄: sodium sulfate; Tris: tris(hydroxymethyl) aminomethane.

Table 2. Mean and standard deviation (SD) values of complex modulus (E^*) (GPa) and $\tan(\delta)$ at experimental ionomer-dentin interfaces under *in vitro* chewing and bruxism events.

	ZONES	GIC (Ketac-Bond)		RMGIC (Vitrebond)	
		CM (E^*)	Tan (δ)	CM (E^*)	Tan (δ)
MECHANICAL LOADING Unloaded	GI	70.30 (5.43) a1*	0.14 (0.02) a1	49.76 (8.16) a1	0.17 (0.05) a1
	HL	146.69 (22.39) b1*	0.19 (0.01) b1	39.96 (11.96) a1	0.16 (0.03) a1
	BHL	79.61 (18.04) a1*	0.10 (0.01) c1*	34.12 (7.98) a1	0.22 (0.06) a1
	ID	67.94 (8.72) a1*	0.14 (0.02) a1*	30.09 (8.83) a1	0.33 (0.04) b1
Sine	GI	43.95 (11.03) a2	0.10 (0.09) a1*	50.77 (13.45) a1	0.22 (0.01) a1
	HL	40.44 (1.19) a2*	0.23 (0.02) b2*	168.51 (8.27) b2	0.05 (0.02) b2
	BHL	27.33 (2.67) b2*	0.30 (0.02) c2*	136.78 (7.74) c2	0.10 (0.02) b2
	ID	22.10 (1.33) c2*	0.35 (0.03) c2*	124.31 (8.34) d2	0.18 (0.02) a2
Hold 24h	GI	37.37 (10.52) a2	0.20 (0.05) a12	28.63 (4.49) a2	0.17 (0.05) a1
	HL	23.94 (2.60) b3*	0.39 (0.08) b3*	40.61 (9.57) a2	0.23 (0.04) a1
	BHL	22.8 (2.74) b2	0.46 (0.09) b3*	34.94 (10.15) a1	0.26 (0.05) a1
	ID	24.92 (7.99) ab2	0.39 (0.06) b2*	30.1 (5.40) a1	0.32 (0.03) a1

Abbreviations: GIC: Glass-ionomer cement, GI: Glass ionomer, HL: Hybrid layer, BHL: Bottom of hybrid layer, ID: Intertubular dentin, CM: Complex modulus, RMGIC: Resin-modified glass-ionomer cement.

Same lower case letters indicate no differences between the distinct zones in the same glass ionomer and load cycling procedure group. Same numbers indicate no differences among load cycling procedures when the same glass ionomer was used. * indicates differences between both glass ionomer groups at the same interdiffusion zone when the identical load cycling procedure was carried on.

Table 3. Raman analysis of mineral and organics components at bonded glass ionomer cements- dentin interfaces.

A		GIC (Ketac Bond)									
		MINERALS				ORGANICS					
MECHANICAL LOADING	ZONES	Relative Presence of Mineral Phosphate [961]		Crystallinity MMR	FWHM Phosphate	Normalization Phenyl [1003]	Crosslinking Pyridinium [1032]	Nature and secondary structure of collagen			Ratio A- I/ A-III
		Peak	Area					A-III [1246- 1270]	CH ₂ [1450]	A-I [1655- 1667]	
Unloaded	HL	4.65	91.03	1.80	14.90	0.93	0.13	23.01	2.58	3.74	0.16
	BHL	13.86	351.14	5.37	19.35	1.28	0.03	18.12	2.58	2.55	0.14
	Dentin	63.08	1598.33	13.99	19.34	2.13	0.87	10.50	4.51	2.93	0.28
Sine	HL	17.97	379.96	6.94	16.12	1.00	-0.18	14.78	2.59	2.51	0.17
	BHL	39.97	844.89	9.70	16.12	1.63	0.47	10.14	4.12	2.88	0.28
	Dentin	80.42	2037.79	15.92	19.34	2.58	1.08	10.46	5.05	4.01	0.38
Hold 24h	HL	22.14	561.15	4.79	19.35	1.88	1.82	17.50	4.62	2.78	0.16
	BHL	36.73	931.21	8.11	19.35	1.66	1.13	12.11	4.53	2.60	0.21
	Dentin	58.57	1238.51	12.54	16.13	1.92	1.33	10.41	4.67	2.84	0.27
B		RMGIC (Vitrebond Plus)									
Unloaded	HL	14.05	356.22	2.17	19.35	1.49	0.74	24.41	6.48	1.52	0.06
	BHL	51.77	1312.08	10.63	19.35	1.80	0.16	11.55	4.87	3.20	0.28
	Dentin	83.31	2111.59	18.07	19.35	2.56	0.68	10.49	4.61	2.24	0.21
Sine	HL	33.45	847.75	7.35	19.35	1.57	0.55	14.09	4.55	2.35	0.17
	BHL	59.19	1500.17	10.48	19.35	1.89	0.11	11.55	5.65	4.22	0.37
	Dentin	73.62	1865.95	23.60	19.35	2.43	0.33	8.98	3.12	2.05	0.23
Hold 24h	HL	36.3	767.26	8.60	16.12	1.27	0.45	13.58	4.22	1.94	0.14
	BHL	53.83	1137.89	11.96	16.12	1.83	1.34	11.71	4.50	2.03	0.17
	Dentin	56.74	1199.4	9.85	16.12	1.71	1.43	13.17	5.76	3.20	0.24

HL: Hybrid layer; BHL: Bottom of hybrid layer; A: amide; MMR: Mineral/Matrix (CH₂) Ratio; FWHM- Full-width half-maximum. Peaks positions are expressed in cm⁻¹.

Figure 1

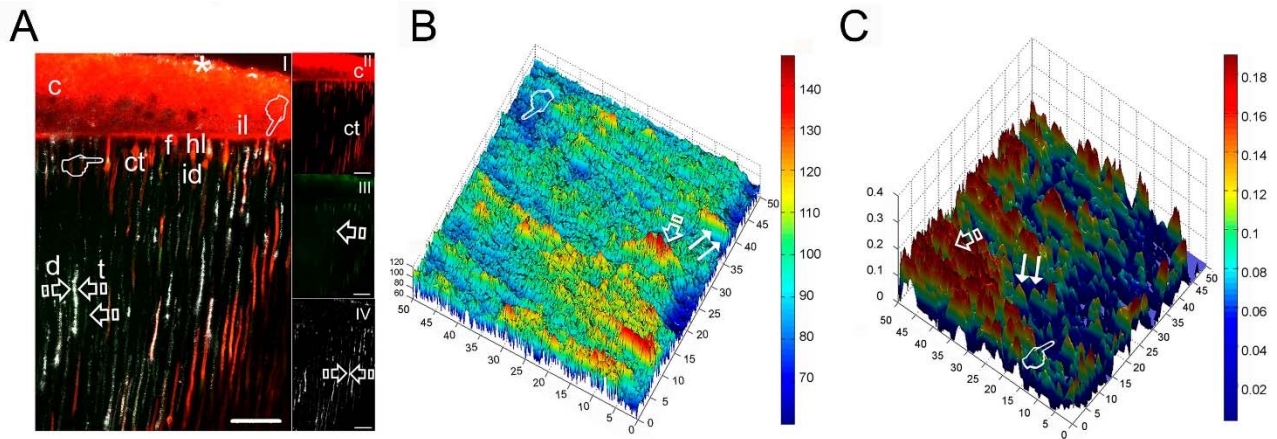


Figure 1. **A**, CLSM images (reflexion/fluorescence) showing the interfacial characterization and micropermeability of the glass ionomer cement Ketac Bond/dentin interface, unloaded. A weak pattern of micropermeability within the dentinal tubules (t) (arrows) and at the Rhodamine B-labeled cement (c) (asterisk), but scarce pattern of micropermeability at the intermediate layer (il) may be observed at **A·I**, immediately adjacent to the hybrid layer (hl). Rhodamine-B has also diffused laterally through the affected tubular walls and mixed with the fluorescein, exhibiting a light spectral overlap (yellow) (pointers) in the emission of profile of both dyes (red and green). Wide fusiform-shaped cement tags (ct) are showing underneath the cement layer, and funneling in some specific locations (f) at the cement-dentin interface (scale bar: 25 μm). In the CLSM image captured in fluorescence mode and imaged with fluorescein (**A·III**), a discrete dye sorption throughout the dentinal tubules is detected. The presence of dye in the restorative material indicates the micropermeability of the interface (scale bar: 25 μm). It is also possible to observe a cement layer characterized by the presence of many cement tags (ct) when imaged with Rhodamine (**A·II**), underneath the cement layer (Scale bar: 25 μm). This interface is also characterized by a moderate reflective signal inside the dentinal tubules, in the form of highly fluorescent structures (faced arrows) (**A·IV**) (scale bar: 25 μm). c, cement layer; d, dentin; ct, cement tags; f, funneling; id, intertubular dentin; il, intermediate layer; t, dentinal tubules. **B**, 3-D contour map of the complex modulus (E^*) distribution in dentin samples treated with Ketac Bond, unloaded. In the color scheme shown, the redder color corresponds to the highest values of the locally measured complex modulus E^* , *i.e.*, the major resistance to deformation. E^* ranged from 67.94 (dentin) (pointer) to 146.69 GPa (hybrid layer), where acute peaks of higher intensities were localized (arrow). The biggest gap among structures appears between the hybrid layer and dentin (78.75 GPa of difference) (double arrows). **C**, 3-D contour map of the tan delta (δ), distribution in dentin samples treated with Ketac Bond, unloaded. In the color scheme shown, the redder color corresponds to the locally measured highest values of tan delta (δ). Tan (δ) ranged from 0.10 (bottom of the hybrid layer) (pointer) to 0.19 GPa (hybrid layer) (arrow), where the lowest proportion of energy available, at this location, was concentrated. Between both of them, a zone of low energy dissipation was created (double arrows).

Figure 2

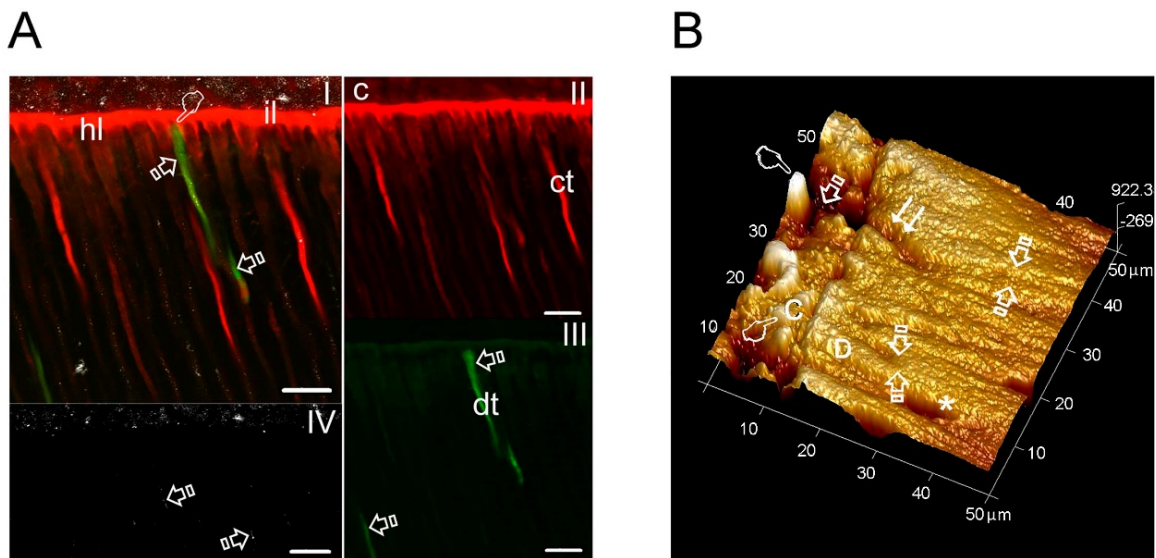


Figure 2. A, CLSM images (reflexion/fluorescence) of the interfacial characterization and micropermeability of the glass ionomer cement Ketac Bond/ dentin interface, loaded in hold 24 h waveform are shown. Null signs of nanoleakage are observed at this projection (A·I), where both scarce penetration of fluoroscein throughout the dentinal tubules (arrows) and water sorption within the thickness of the hybrid layer (hl) (pointer) can be seen. The intermediate layer was not affected by dye sorption (scale bar, 10 μm). A·II exhibits a cement layer characterized by the presence of many funneled cement tags (ct) when imaged with Rhodamine, are underneath the cement layer (c) (Scale bar: 10 μm). In the CLSM image captured in fluorescence mode and imaged with fluorescein (A·III), a discrete dye sorption throughout some dentinal tubules (dt) is detected (arrows). The absence of dye in the restorative material indicates the null micropermeability of the interface (Scale bar: 10 μm). This glass ionomer cement infiltration is also characterized by an indiscernible reflective signal inside the dentinal tubules, in the form of faintly fluorescent structures (arrows) (A·IV) (Scale bar: 10 μm). c, cement; ct, cement tag; dt, dentinal tubules; il, intermediate layer. B, Topographic mapping of dentin infiltrated with Ketac Bond after loading in hold 24 h, obtained by AFM. Tight adaptation between cement and dentin was observed. Some voids and artifactual cracks in the polyalkenoate matrix (arrow) and multiple particles (pointers) are also shown. Minerals allowed a restricted display of the tubule entrances (double arrows) or a complete sealing of the lumen of tubules (faced arrows). Peritubular dentin appeared strongly remineralized (asterisk).

Figure 3

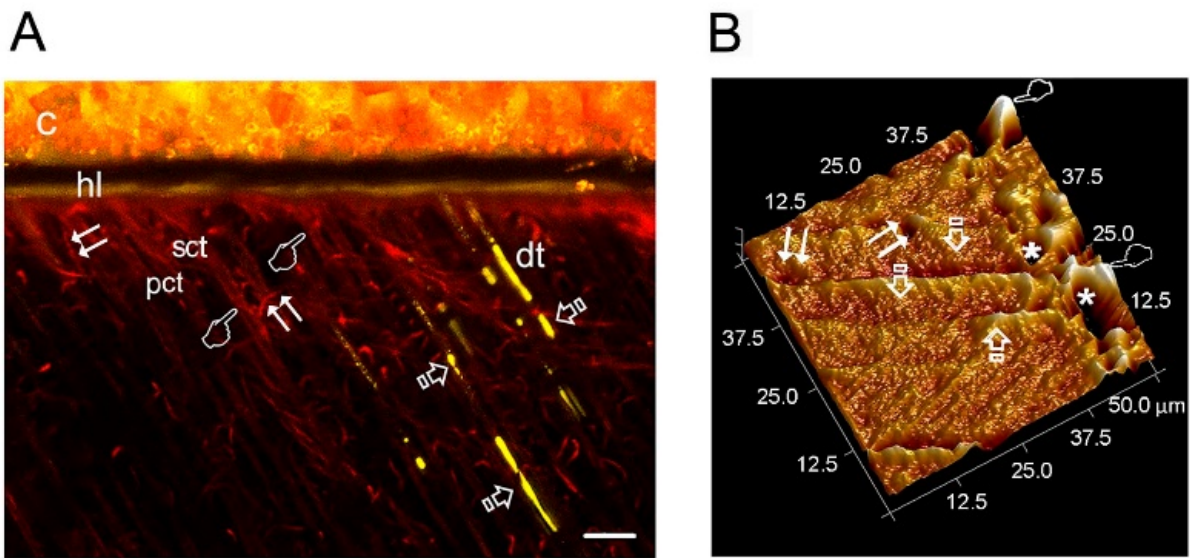


Figure 3. A, CLSM single-projection image disclosing the fluorescent calcium-chelator dye xylene orange, showing the interfacial characterization of RMGIC Vitrebond Plus-dentin, and loaded in sine waveform. It exhibits mineral deposition visualized within the hybrid layer (hl) and along some dentinal tubules (dt) (arrows). Note the presence of intact principal (pct) (pointer) or secondary (sct) (double arrows) cement tags imaged in Rhodamine excitation/emission mode (scale bar, 10 μm). c, cement; dt, dentinal tubules; hl, hybrid layer; ct, cement tags. **B**, Topographic mapping of a dentin interface infiltrated with Vitrebond Plus after load cycling in sine waveforms, obtained by AFM. Tight adaptation between cement and dentin was observed. Some voids caused by fillers lost (asterisks) and particles (pointers) within the cement layer were also shown. Peritubular dentin is completely mineralized (arrows), and the mineral formations only allowed a restricted display of the tubule entrances (double arrows).

Supplemental figures

Figure S1. Schematic illustration of the GIC-dentin interface. GIC, glass ionomer cement; RMGIC, resin modified glass ionomer cement; HL, hybrid layer; BHL, bottom of hybrid layer; AL, Absorption Layer; IL, Intermediate layer; ct, cement tag; dt, dentinal tubule.

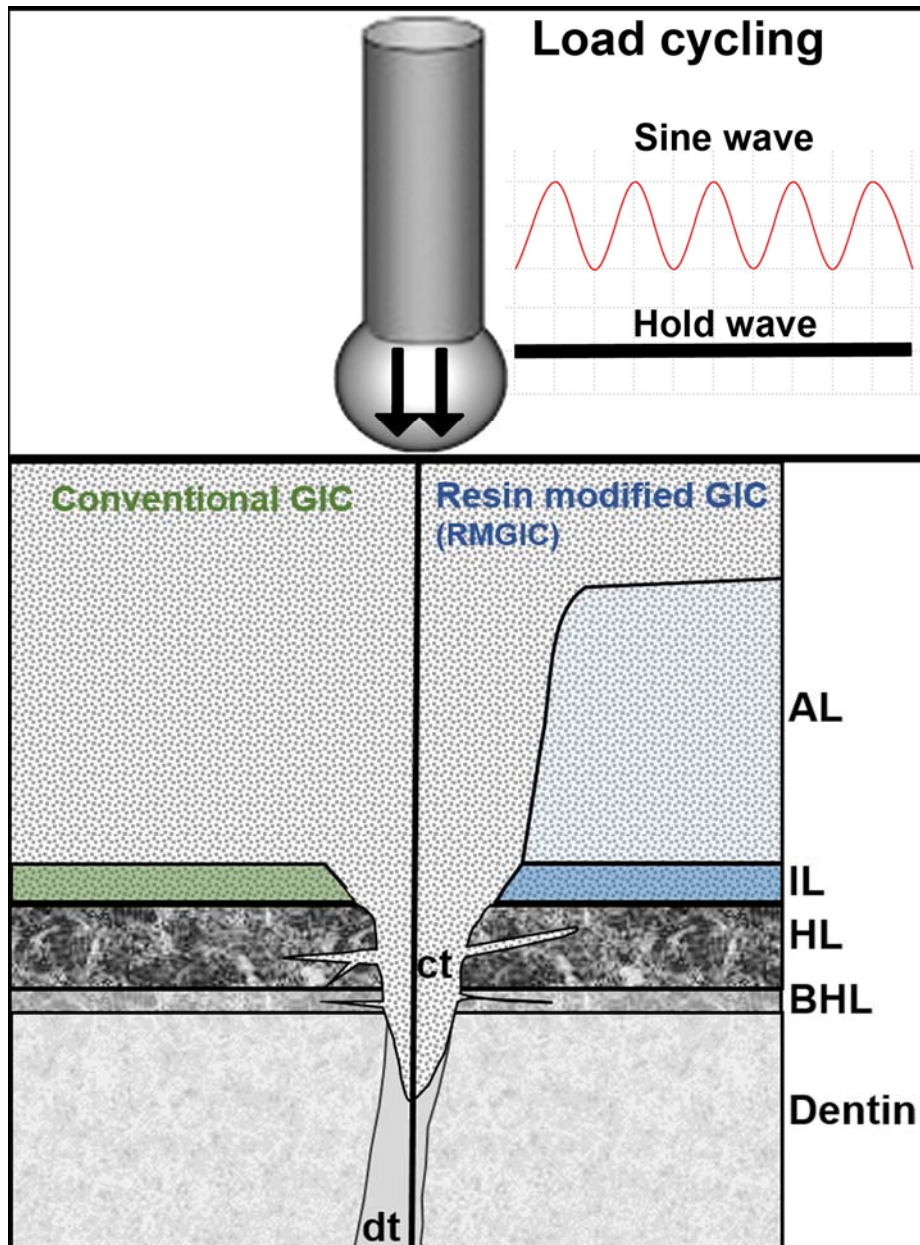


Figure S2. CLSM images (reflexion/fluorescence) showing the interfacial characterization and micropermeability of Vitrebond Plus/dentin interface, loaded in hold 24 h waveform. A strong pattern of micropermeability within the dentinal tubules (dt) (arrow) and at the Rhodamine B-labeled cement (c) (asterisk) may be observed. **A**, this indicates the porosity of the interface, as a clear dye sorption throughout its thickness is shown. Rhodamine-B permeated from the pulp diffused laterally through the affected tubular walls and mixed with the fluorescein, exhibiting a light spectral overlap (yellow) (pointers) in the emission of profile of both dyes (red and green). The absorption layer (al) was detected within the body of the material immediately adjacent to the dentin. This cement infiltration is also characterized by a scarce presence of thin cement tags, and by moderate reflective signal inside the dentinal tubules, in the form of weakly fluorescent structures (double arrows) (scale bar, 25 μm). **B**, Topographic mapping of dentin infiltrated with Vitrebond Plus after load cycling in hold 24 h, obtained by AFM. Extraction of fillers originated multiple voids at the cement surface (asterisks). A constant lack of intimate interactions, hindering an accurate adaptation between cement and dentin was denoted after the presence of a gap in the middle (pointers). Dentinal tubules appeared permeable (arrows) and partially occupied by mineralized cement tags (double arrows), and surrounded by evident peritubular dentin rings (faced arrows).

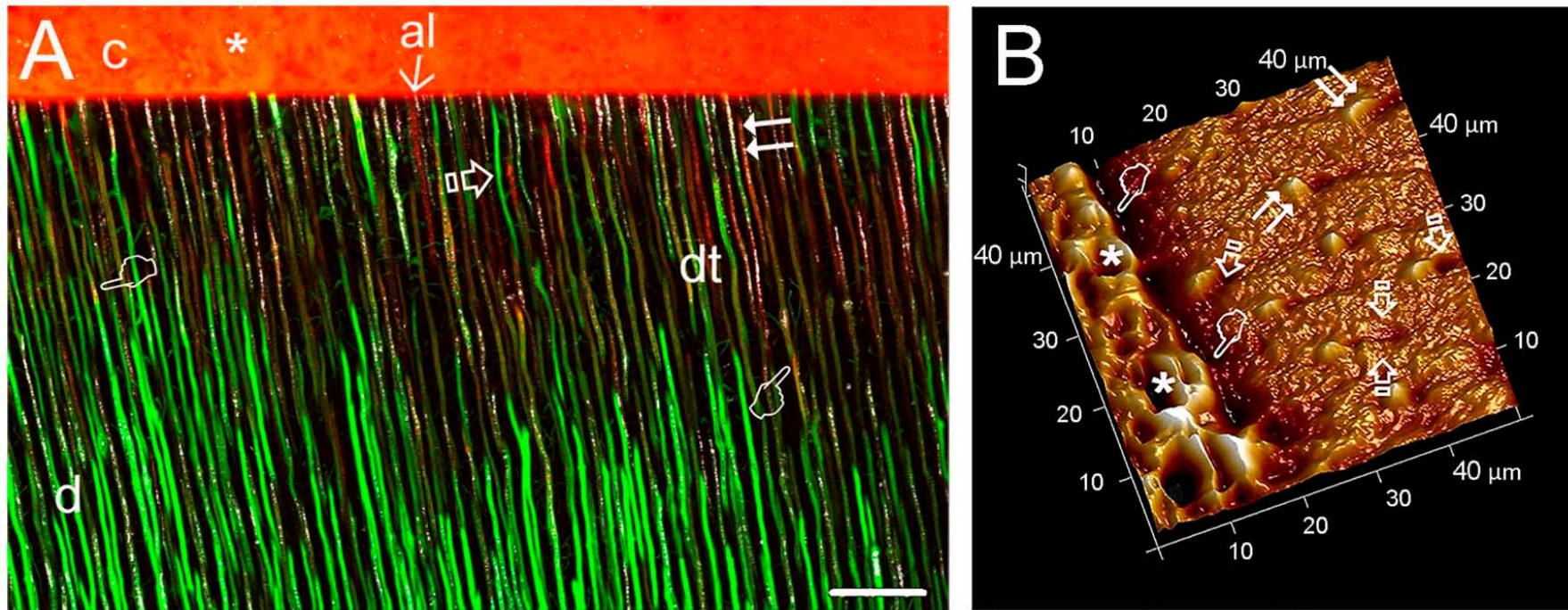


Figure S3. 2D micro-Raman maps of the phosphate peak (961 cm^{-1}) intensities at the Ketac Bond-dentin bonded interface unloaded (A), load cycled in sine (B), and in hold 24 h (C) waveforms. In the color scheme shown the redder color corresponds with higher values of the locally measured phosphate peak (961 cm^{-1}) intensities.

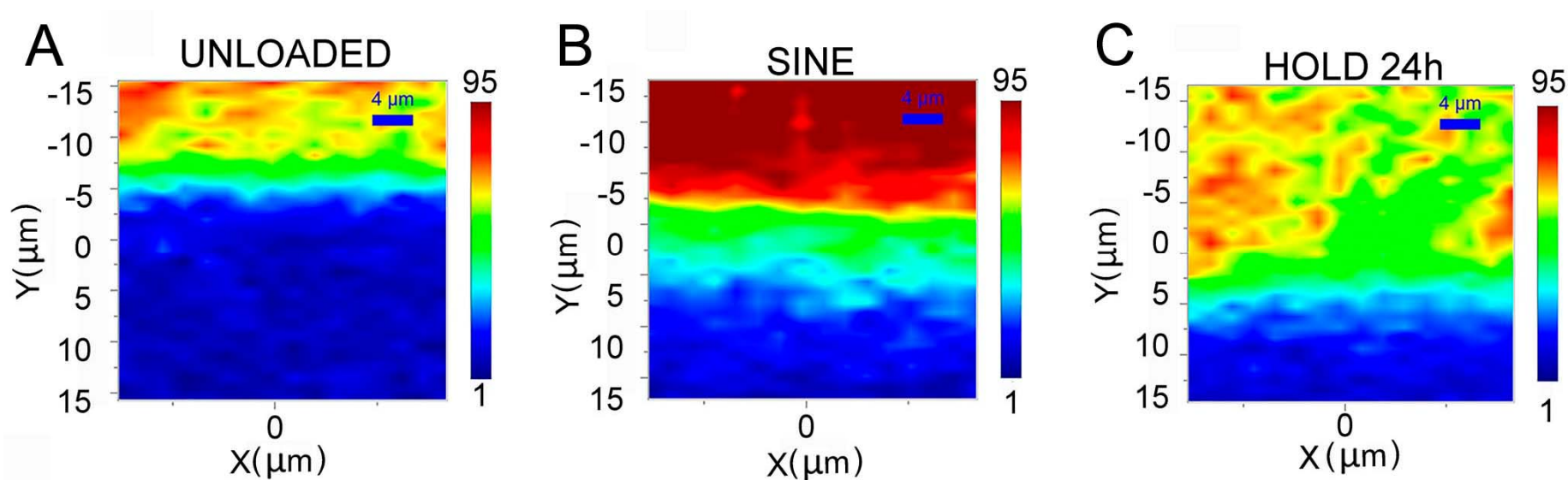


Figure S4. Topographic mapping of dentin infiltrated with Ketac Bond load cycled with sine waveforms, obtained by AFM. Extraction of fillers originated multiple voids at the cement surface (asterisks), though many others particles remained within the body of the material (P). An extended interface characterized by a lack of accurate adaptation between the cement and the dentin was observed (arrows). The vast majority of dentinal tubules appeared totally occluded with cement tags and/or mineral deposits (pointers). Peritubular dentin appeared strongly remineralized (faced arrows). Stick-slip images, in radial direction, of nucleated minerals resulted observable at the intertubular dentin (double arrows). Strong processes of intertubular and intratubular mineralization were also observed (faced double arrows). P, particles.

